# Chapter 9
# Recurrence Analysis of Cardiac Restitution in Human Ventricle

**Humberto Arce, Ayari Fuentes and G. Hortensia González**

**Abstract**  The cardiac restitution curve describes functional relationships between diastolic intervals and their corresponding action potential durations. Although the simplest relationship is that restitution curves are monotonic, empirical studies have suggested that cardiac patients present a more complex dynamical process characterized, for instance, by a non-monotonic restitution curve. The purpose of this chapter is to analyze the dynamical properties of a non-monotonic cardiac restitution curve model derived from previously published clinical data. To achieve this goal, we use Recurrence Quantitative Analysis combined with Lyapunov exponents and Supertrack Functions in order to describe the complex dynamics underlying non-monotonic restitution curves. We conclude by highlighting that a consequence of the advanced complex dynamics that emerges from the aforementioned non-monotonicity, is the increasing risk of alternant rhythms.

## 9.1  Introduction

Cardiovascular accidents are a major cause of death worldwide. Among the diverse risk indicators, a significant one is the appearance of T-wave amplitude alternans on electrocardiograms consequence of a beat-to-beat oscillation on the intracellular *action potential duration* (APD) [1]. APD alternans have been studied using the *electrical restitution curve* or *cardiac restitution curve* (CRC) since the 70's of the

H. Arce (✉) · G.H. González
Laboratorio de Biofísica de Sistemas Excitables, Facultad de Ciencias,
Universidad Nacional Autónoma de México, Mexico, Mexico
e-mail: harce@ciencias.unam.mx

G.H. González
e-mail: hortecgg@ciencias.unam.mx

A. Fuentes
Centro de Ciencias Genómicas, Universidad Nacional Autónoma de México,
Mexico, Mexico
e-mail: ayarifh@ccg.unam.mx

last century, an approach based on studying the interaction between the action potential duration and the *diastolic interval* (DI) [2, 3]. The simplest interpretation is that the APD depends exclusively on the previous DI because cardiac cells only have a cycle length time to recover its ionic kinetics [4, 5]. However, theoretical and experimental results have suggested a memory effect that depends not just on the immediate previous cycle [6, 7].

The relevance of this approach is partly a consequence of results showing that the slope of the CRC can be modulated by pharmacological interventions [8–11] or by changing the propensity for ventricular fibrillation in cardiac preparations through pacing protocols [12–16]. In general, modeling studies consider the CRC as a monotonically-growing exponential curve [8, 13, 17–20] and, as a consequence, if the slope of the APD adaptation is higher than one, a reduction on the stimulation interval eventually leads to a period-doubling bifurcation [2, 21]. Indeed, a CRC slope >1 amplifies APD alternans and therefore it can lead to fibrillatory rhythms. For this reason, electrical restitution curve analysis has become an important tool for cardiac risk prediction [4, 6, 10, 13]. However, since 1975 multiple empirical studies have reported the occurrence of non-monotonic curves in different cardiac assays [11, 22, 23]. In particular, for the human ventricle, Franz and colleagues found in 1985 the existence of a shoulder or local maximum in the CRC [4, 23]. These results were exhaustively verified in 2005 by Yue et al. [24] using a S1–S2 stimulation protocol. Furthermore, their array of non-contact electrodes revealed CRC with diverse profiles in contiguous cardiac cells of the same patient; from purely monotonic to a non-monotonic profile with a very pronounced local maximum, a feature illustrated in Fig. 9.1a.
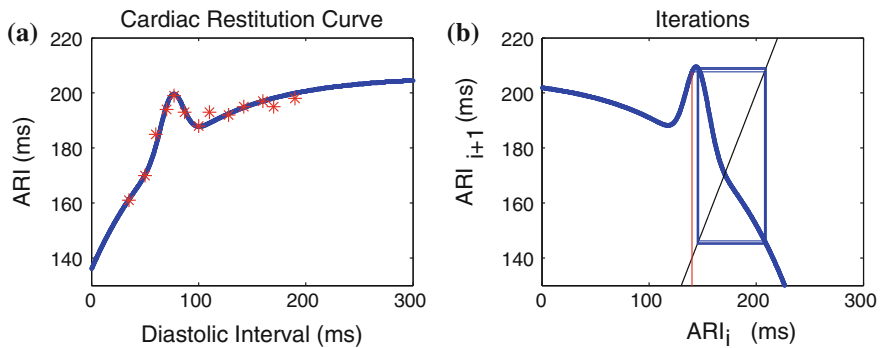


**Fig. 9.1 Cardiac Restitution Curve with Local Maximum** (CRC-LM). **a** the *red asterisks* correspond to 13 experimental points taken from Yue et al. [24] obtained using a S1-S2 stimulation protocol; the *blue* trace is the function that we used to fit the data based on the addition of an exponential and a Gaussian functions. Activation Recovery Interval (ARI) is an indirect measurement of the intracellular APD. DI denotes the Diastolic Interval and represents the resting time between activations. **b** iteration map used to obtain the time series (see methods for an extended explanation)

In this work, we show that the presence of a local maximum in a human data-driven CRC model can considerably advance the alternant behavior and, as a result, the *bifurcation diagrams* (BD) for these CRC are highly complex. Our analysis is based on a methodological extension of recurrence plots analysis known as *recurrence quantitative analysis* (RQA) based on the following indexes: *recurrence times of the second type* (T2), *recurrence rate* (RR), the *maximum diagonal length* (Lmax) and the *maximum vertical length* (Vmax). We then compare the predictions obtained using RQA with the results obtained using Lyapunov exponents. Using both approaches we demonstrate how an increment in the local maximum height has the effect of increasing the complex region size in the BD, as well as the magnitude of the alternans. Finally, we describe the different transitions observed.

## 9.2   Methods

### 9.2.1   Generation of Time-Series

In this chapter we propose a model based on data obtained by Yue et al. [24] who used an experimental protocol that introduces an extracellular electrode array into the right or left ventricle of a cardiac patient. This protocol allows the authors to measure a time interval equivalent to the intracellular APD known as the *activation recovery interval* (ARI). ARI was measured between the time of $(dV/dt)_{min}$ of the QRS and the $(dV/dt)_{max}$ of the T-wave on the unipolar electrograms of the ventricular endocardium employing a S1–S2 stimulation protocol based on a constant stimulation period maintained for 2 min, with an extra stimulus intercalated at a different time point [24].

For the purpose of this chapter we will define the CRC with local maximum as CRC-LM and estimate the experimental points in Fig. 9.2 panel C of Yue et al. [24]. We discarded the two shorter ones because they overlap with a third experimental point. Then, in order to fit the 13 remaining points, we added a Gaussian function to an exponential curve matching the local maximum position with the corresponding experimental maximum, as illustrated in Fig. 9.1a. We then obtain the following semi-quantitative function

$$ARI = 206 - 70\exp(-DI/78) + 20\exp(-((-75+DI)2/220)) \qquad (9.1)$$

where the Gaussian coefficient (third term) is representative of its height, *h,* which in (9.1) corresponds to 20. Note that when this parameter equals zero the CRC is monotonic, and therefore here we are interested in changing its value to evaluate the CRC-LM deviation from the well-characterized behavior of monotonic curves.

We then consider a series of stimuli applied with a given period denoted by *P*. The effect of each stimulus will be to generate a voltage deflection with a given
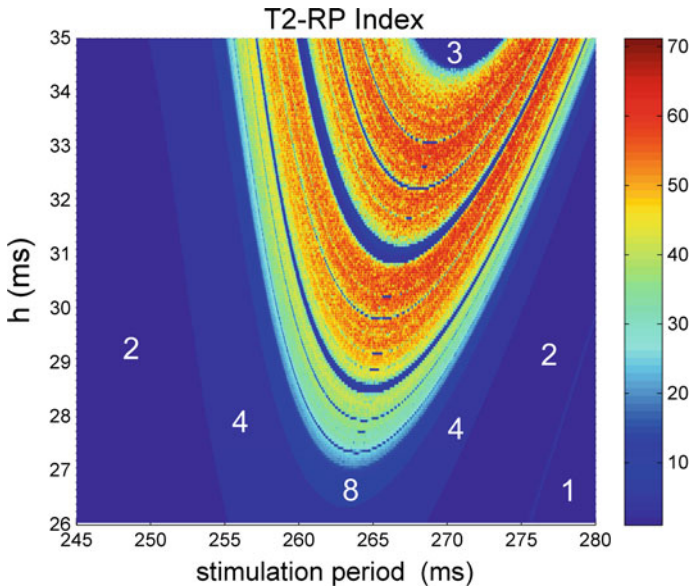
**Fig. 9.2 Biparametric BD using T2**. T2 was obtained from RP as index. N-Rhythms are longer as h is increased. *White numbers* indicate the basic rhythm observed in the corresponding band

$\text{ARI}_i$ followed by a diastolic interval, $\text{DI}_i$ and therefore we obtain the following constant value of P for each series of stimulus:

$$P = \text{ARI}_i + \text{DI}_i. \tag{9.2}$$

Now, (9.1) states that each ARI depends on the previous DI so, we can define a discrete map, denoted as F, such that

$$\text{ARI}_{i+1} = F(\text{DI}_i) \tag{9.3}$$

and thus from (9.2) we obtain

$$\text{ARI}_{i+1} = F(P - \text{ARI}_i). \tag{9.4}$$

So, in order to produce a time-series for a given pair P and *h,* we only need to propose an initial ARI and perform the necessary iterations. Figure 9.1 panel B shows the results obtained with $h = 30$, $P = 220$ and with an initial ARI of 140 ms. Note that after a short transient interval, a 2-period rhythm is achieved, that is, ARI values repeat every two other pulses. Indeed, N-rhythm is defined as repeated pattern every N elements, a pattern that depends on *P*. Longer periods move F to the right-hand side and the shorter ones to the left, displacing the intersection of F with the identity line. Then we have that each time-series depends on *h* for a given CRC-LM and *P*.

## 9.2.2 Dynamic Bifurcation Diagrams

We used three approaches to study the CRC-LM curves. Initially, we applied a method proposed by Trulla et al. [25] to obtain the BD and RQA indexes very quickly. This method is based on incrementing in small steps the bifurcation parameter before every new iteration of F. First, we obtained the BD for $h$ with values ranging from 0 to 35 ms with steps every 0.05 ms. For each $h$, a modified ARI time-series was generated starting from $P = 100$ ms with increments of 0.001–300 ms. Once identified the region of interest inside the $P \times h$ space, we calculated the T2-RQA index and the maximum Lyapunov exponent in the region defined by $h$ from 26 to 35 ms with 0.05 ms steps and $P$ between 245 and 280 ms with 0.0001 ms steps. The time-series consists of 350,000 points that were sub-divided in 500-point blocks in order to calculate T2 and the higher Lyapunov exponent. Recurrence times of the second type (T2) were proposed by Gao [26] and correspond to the recurrence time remaining after the sojourn times in a specified epsilon are discarded. Here we obtained T2 using CRP-TOOLS (http://tocsy.pik-potsdam.de/CRPtoolbox/).

To calculate Lyapunov exponents, we used the logarithm of the derivatives product of F in each element of the 500 points orbit [27], moving along the time-series with 10-point steps. Based on previously published results [25, 26], we defined D = 2 and t = 1, as well as used the Euclidean norm and epsilon = $2^{-5}$. Then, to compare our results with the standard stationary method, we obtained time-series for each $P$ and $h$ with 2,000 values in each case, but calculated T2 and the Lyapunov exponent based on the last 500 values of the time-series.

In the second part of this study, we followed the evolution of the system as $h$ changes using the stationary procedure to estimate the *recurrence rate* (RR), the *maximum diagonal length* (Lmax) and the *maximum vertical length* (Vmax) from the time-series. These indexes are part of the RQA proposed as an extension of the Recurrence Plots [28, 29] where RR quantifies the percentage of recurrent points falling within the specified epsilon, Lmax is the length of the longest diagonal line segment in the plot (excluding the main diagonal line of the identity) and Vmax measures the length of the longest vertical line in the RP. This index was proposed later [30, 31] and reveals information about the time duration of the laminar states, allowing the investigation of intermittency possible.

Finally, in order to study the evolution of laminar zones, we obtained the *normalized recurrence frequency* (NRF) with a maximum that coincides with the *super track functions* (STF) for the CRC-LM under consideration. NRF is a histogram obtained for each $P$ that measures how a time-series recurs to some particular value. The extreme ARI values in all the BD were identified; these intervals were divided in 0.001 ms bins to count the ARI values and normalized to the highest frequency found. The obtained values allowed us to analyze the most visited frequency bands in the BD. STF were obtained following Oblow [32]. In the map defined by F the invariant point corresponds to the maximum point, so we considered this value as the first $s_1$ function that results constant. The following $s_n$ are then the $n$-th iteration value obtained from the map for each BD parameter, in our case $P$.

## 9.3 Results

### 9.3.1 Dynamic Method

The most relevant result we found is that, for a clinically and physiologically relevant context, the presence of a local maximum markedly advances the initiation of alternans. Furthermore, as alternans are cardiac risk predictors, we conclude that CRC-LM increases the risk for arrhythmia. We studied local maxima from 0 to 35 ms in height, with increments of 0.05 ms and, for each $h$ studied, $P$ was taken as a bifurcation parameter starting in 100 ms and going to 300 ms with 0.001 ms steps. When $h = 0$ the CRC corresponds to a monotonic curve and alternans appear when $P$ is reduced to 121.3 ms. Moreover, increasing $h$ leads to a new alternans zone. When $h = 10.5$ ms we see that the system is in a 2-rhythm alternant pattern between 244 and 246 ms. A larger value of $h$ has the effect of increasing this region and therefore its behavior is more complex. For $h = 11$, the alternans region spans from 243 to 250 ms, while for $h = 35$, from 223.7 to 285.9 ms. To carefully analyze this alternans region, we defined the $h$ interval between 26 and 35 ms and $P$ from 245 to 280 ms and calculated T2 as well as the higher Lyapunov exponents using Trulla et al.'s method [25] with 0.0001 ms variations in the bifurcation parameter.

Figure 9.2 presents the results obtained for T2 index. The period $P$ (in ms) is on the horizontal axis, and the height $h$ (also in ms) on the vertical axis. T2 is indicated by the color bar at right. The general shape of the plot is of colored bands similar to upwards parabolas barely shifted to the right. As $h$ grows, the rhythms (denoted with white numbers) move simultaneously inward from the left and right border, and new N-rhythms emerge. This pattern is interrupted by shorter periodicity bands (shown in blue).

Figure 9.3 shows the results obtained for the Lyapunov exponents. For clarity purposes, exponents $<-0.2$ have been truncated. Interestingly, this Figure has the same bands pattern as those shown in Fig. 9.2. The frontiers between 2, 4 and 8-rhythms are highlighted because Lyapunov exponents in these zones are very close to zero. We can see that zones with positive exponents (corresponding to chaotic regions) are related to zones with T2 higher than 20 in Fig. 9.2. In this Figure, we sketched a couple of white dotted horizontal lines; the first one in $h \sim 26.9$ ms is the highest limit to the periodic behaviors. It is important to notice that in the region between the two lines, chaotic behavior without laminar states can be present, while laminar states exist only above the higher line.

### 9.3.2 The Stationarity Method

For each time-series obtained with this procedure, the last 500 points were taken into account in order to obtain the RQA indexes (RR, Lmax and Vmax). Figure 9.4 illustrates the behavior of the system in the period-doubling bifurcation zone, from
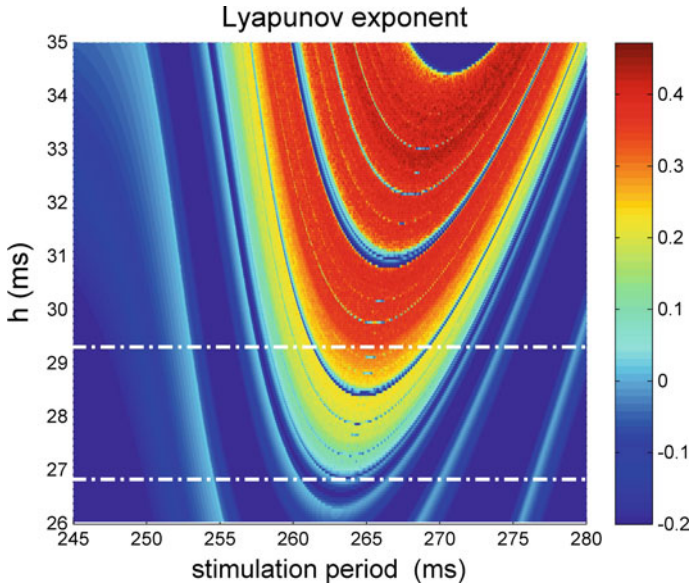
**Fig. 9.3  Biparametric BD for Lyapunov exponent**. Periodic states are found exclusively under the *bottom white line*, while chaos without laminar states can be found between both *dotted white lines*. Above the *top dotted white line* we can find chaos with laminar states. To recognize them we used the Lmax and Vmax evolution, explained afterwards in the text and shown in Figs. 9.4, 9.5 and 9.6

$h = 10.5$ up to approximately $h = 26.95$. For $h = 10.5$, the alternans zones is only of 2 ms. Interestingly, alternans magnitude calculated as the difference between highest and shortest ARI is 1.4 ms. In Fig. 9.4a shows the BD for $h = 20$ ms. Although alternans are still between 2-period rhythms, their magnitude has grown to 37.5 ms (and therefore arrhythmia risk is increased) and the width of the region where they exist is of 40 ms. We can see that alternans magnitude reduces as $P$ grows.

Figure 9.4b displays the typical bubble shape of the BD associated with this system. Increments in $P$ produce period-doubling bifurcations in a sequence 1, 2, 4, …$2n$ where $n$ depends on $h$. As $P$ increases, the inverse sequence $2n$, …4, 2, 1 develops. Figures 9.4c and 9.4d show RR (Fig. 9.4c), Lmax and Vmax (Fig. 9.4d) indexes. The RR inverse is the rhythm value of the corresponding orbits. An Lmax change in short steps is signaling transitions between periodic rhythms.

Figure 9.5 shows the behavior in the $h$ region where chaos without laminar states can exist, an interval that spans from $h = 26.95$ to $h = 29.1$ ms. Figure 9.5a shows the BD for $h = 26.95$ ms, while Fig. 9.5b shows the evolution of Lmax and Vmax with $P$. It can be noted that there is a marked reduction in Lmax which is related to the appearance of chaotic activity, in this case the region has 2 ms in size. In Fig. 9.5c it is shown the BD for $h = 29.1$ ms and from Fig. 9.5d we can infer that
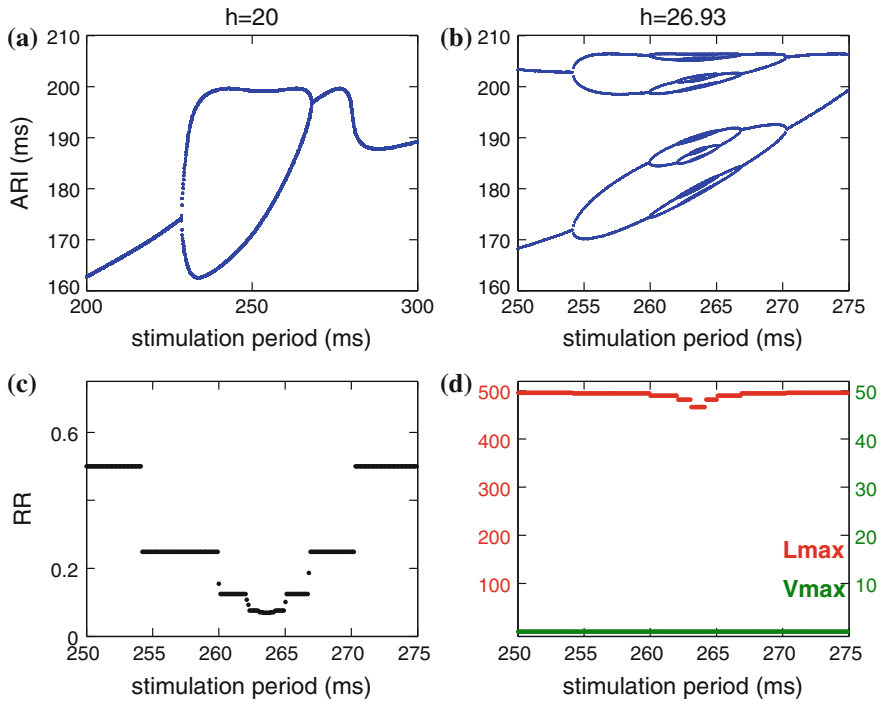
**Fig. 9.4 Periodic Rhythms**. In **a**, two consecutive period-doubling bifurcations are shown, occurring at h = 20 ms. **b** shows two bifurcation cascades from 2 to 32-rhythms and vice versa. **c** shows that recurrence density (RR) reflects the BD rhythms. **d** shows that Vmax = zero because there is not laminarity and Lmax has only small changes corresponding to high order periodic rhythms

chaotic region size increased more than 10 ms. In this case, in the interior of the chaotic region there are clearly distinguishable periodic windows. As Vmax is not different than zero (during the entire $h$ interval) we know that there are no laminar states. The $h$ interval for chaotic behavior and laminar states is from $h = 29.1$ to $h = 35$ ms, the latter being the highest $h$ we considered in this study. Figure 9.6 shows the behavior found in this region.

Figure 9.6a displays the BD with the two chaotic bands that in Fig. 9.5c were unjointed and now partially merged, while Fig. 9.6b shows Lmax and Vmax for $P$ values ranging from 262.2 to 269.3 ms, a region where there are windows with Vmax different from zero and therefore laminar states occur in these windows. To illustrate these states, we produced the corresponding RP for $P = 262.2$ ms that leads to chaotic behavior (only the last 200 points in the time-series were considered in this plot). It is important to mention that here, as in all the cases previously presented, we consider $D = 2$ and $t = 1$. Now, we can see that the observed pattern
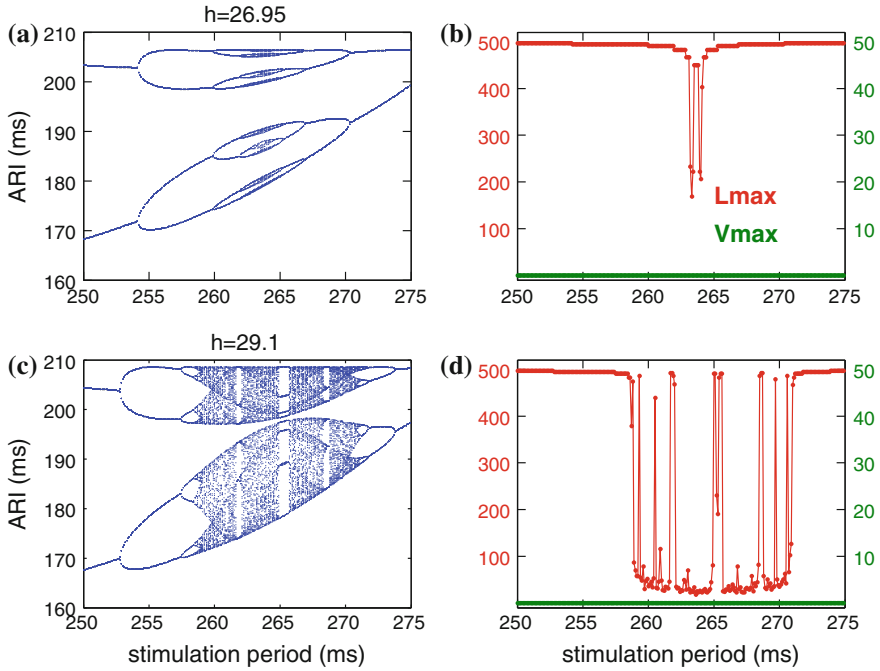
**Fig. 9.5 Chaos without laminar states. a** displays the BD for h = 26.95 ms. **b** shows that for this h there are already chaotic states since Lmax has sudden drops in respect to its value under periodic regimes. **c** shows BD for h = 29.1 ms and **d** indicates that the main effect due to h increase is the expansion of the region presenting chaos, revealed as Lmax index has more frequent drops

is characterized by small diagonals whose length is related with the exponential divergence of their phase space trajectories [31]. Figure 9.6d displays the RP for the last 200 points in the time-series generated when $P = 266.3$ ms. Note how small black blocks can be observed, corresponding to consecutive ARI with similar values.

To follow in detail the evolution of the region that presents laminarity, we calculated the NRF (see methods) for the case h = 30 ms. We see that the highest ARI value is slightly smaller than 210 ms and the lowest is slightly larger than 165 ms. We divided the interval in 45,000 equidistant windows and, for each $P$, counted the amount of elements in every window.

We also produced a histogram for the normalized time-series (with frequency values ranging from 0 to 1). Figure 9.7a shows the ARI when NRF = 1. This plot shows the surrounding lines that contain the two merged chaotic zones. In Fig. 9.7b, the first four STF are superposed to the plot in Fig. 9.7a. We see that the STF and the surrounding lines are in exact correspondence.
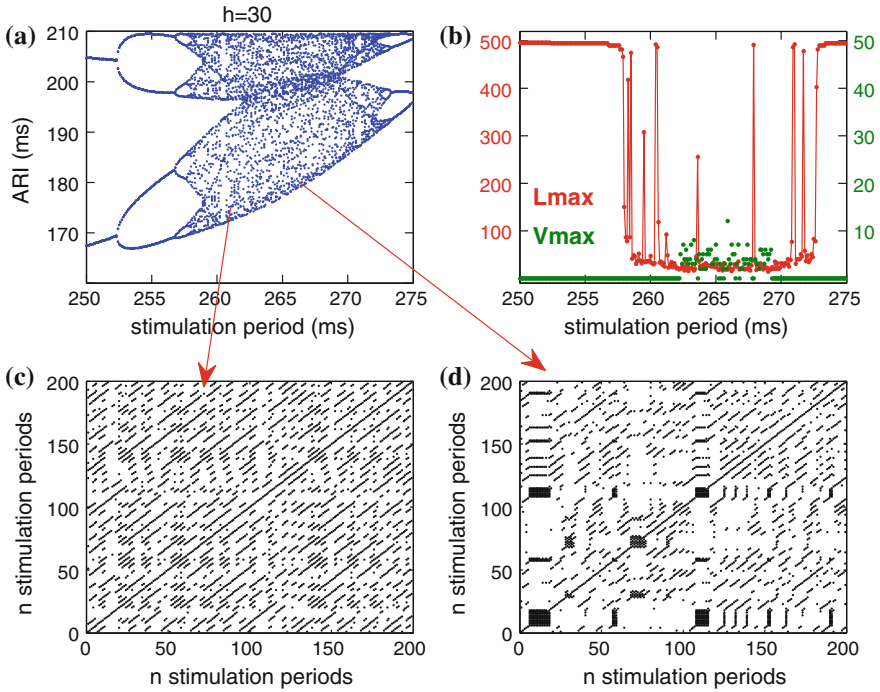
**Fig. 9.6 Chaos with laminar states**. **a** displays the BD for h = 30 ms. Note how in the middle of the plot, two chaotic zones are superposed. **b** shows that this superposition leads to a Vmax different from zero for some values of P. **c** and **d** show the RP built with 200 points, D = 2, delay = 1, epsilon = 0.2. **c** corresponds to P = 262.2 ms where there is chaotic behavior. **d** shows that, for P = 266.3 ms, there are laminar states. Recurrence is calculated after each stimulus

Figure 9.7c displays ARI values with STF > 0.5. Note that it is possible to identify new accumulation lines immersed in the BD; these lines coincide with the next four STF shown in Fig. 9.7d. The STF intersecting points are called star points [32] and we can observe two of them (indicated with black arrows) in Fig. 9.7d.

Finally, we observe that the laminar states occur inside the interval between these two star points. In Fig. 9.8 we show the growth of this inter-star zone with h variation. In Fig. 9.8a we have the case previous to the star point's emergence; in Fig. 9.8b there are already two star points with the intermittence zone between 264.22 and 266.58 ms. For h = 30 ms, shown in Fig. 9.8c, this interval ranges from 262.2 to 267.2 ms. In Fig. 9.8d, for h = 35 ms, the P interval spans from 257.9 to 278.8 ms, and shows a region where 3-period rhythm is present. This region is also observed in the right upper corner of Fig. 9.2. The P intervals for
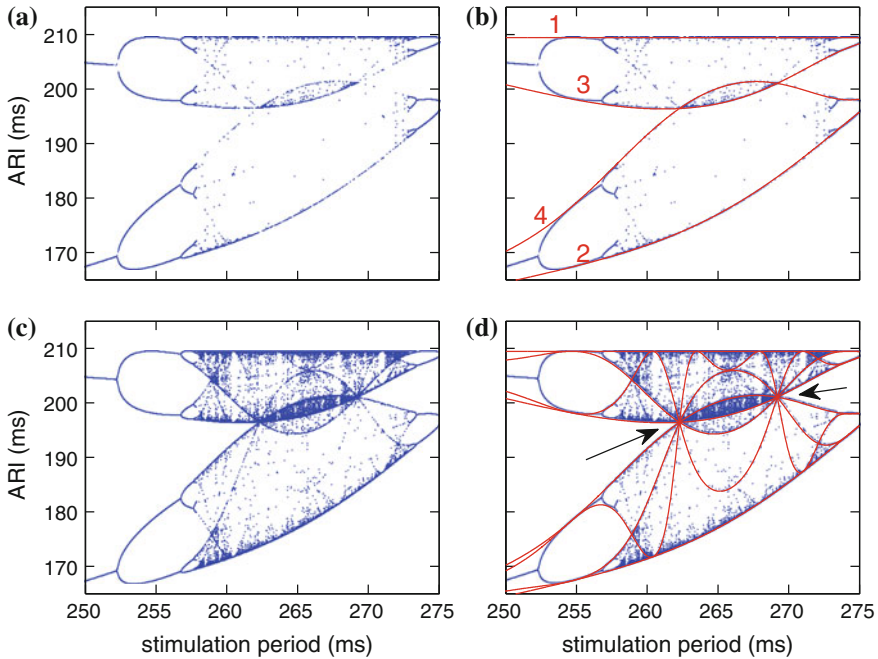
**Fig. 9.7 Super Track Functions**. **a** displays the plot for NRF = 1. **b** shows the superposition of points in **a** with the first four STF. In **c**, points with NRF > 0.5 are shown, while **d** shows the first eight STF superposed to points in **c**. *Arrows* indicate the star points where laminar states can be found in between

these reported laminar states were verified by calculating the corresponding Vmax. A final observation is that if $h = 29.3$ ms and there are not yet star points, there exists a very short laminarity zone ranging from 264.6 to 265.8 ms.

## 9.4  Discussion

CRC has been employed before as a theoretical and experimental tool to study the occurrence of alternans in portions of cardiac tissue or in isolated cardiac cells. The first authors to propose a graphic method to predict this phenomenon were Nolasco and Dahlen [3]. In 1984 Guevara et al. proposed an iteration map over the CRC obtained from the embryonic chick cardiomyocytes [2]. They showed that by reducing the stimulation period, a period-doubling bifurcation was achieved, moving from 1-period rhythm to a 2-period rhythm in the APD. This bifurcation occurred when the fixed-point in the map has a slope equal to 1. Later, it was shown
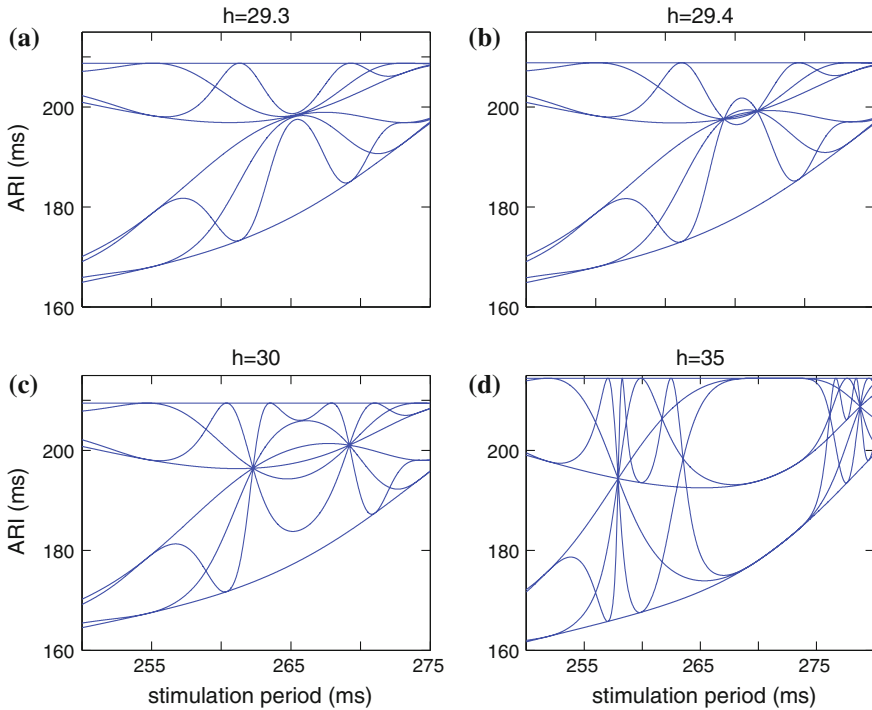
**Fig. 9.8 Laminar states growth**. **a** to **d** show how, as h increases, the region with laminar states (that is, between star points marked in Fig. 9.7) increases

that drugs like verapamil (a calcium channel blocker) modified the slope of the CRC and consequently the bifurcation behavior in cardiac assays [5, 10]. However, other studies have found that, in some cases, the alternant behavior is reached even with slopes less than 1, suggesting that theoretical models should consider further complexities, for instance including memory effects [6, 7, 12].

The experimental results for the human ventricle CRC of cardiac patients obtained by Franz and colleagues, showed the existence of a local maximum in some of the ventricular cells, contiguous to others with monotonic CRC. Furthermore, they showed that inhomogeneous conditions can prevail in the ventricle of a cardiac patient [24]. Although most of the experimental studies can be made in very controlled settings, this is, of course, faraway from clinical conditions [16, 20, 22]. Therefore, exploring different bifurcation scenarios for the onset of alternans in different CRC profiles is still a relevant task.

Here we have modeled the profile of the non-monotonic CRC as the addition of two functions, an exponential and a Gaussian function, adjusting the maximum of the Gaussian function to the local maximum of the experimental curve. We showed that this local maximum leads to an advance in the emergence of alternans of 122.7 ms respect to the observed $P$ in a monotonic CRC. Using analytical tools

derived from RQA, we described how the alternans region is increased as the parameters are varied, as well as how the alternans magnitude and complexity of the system are modified. Also, RP was shown to be a very useful tool to study the complex behaviors nested in the irregular zones. In summary, we found that, as $h$ grows, a period-doubling bifurcation in direct and inverse cascades appears, characterized by chaotic zones without laminar states and subsequently by chaotic zones with laminar states. We showed that the evolution of these regions can be followed-up using the STF built with the orbits obtained from time-series generated from the CRC-LM.

Although to our knowledge there is no experimental data in human ventricle to contrast with our theoretical results, there is a report by Watanabe et al. [11] that qualitatively reproduced our findings employing sheep epicardial strips with a biphasic CRC. Indeed, varying the stimulation period from 200 to 110 ms, the sequence of rhythms observed was 1:1, irregular, 8:8, 4:4, irregular, 2:2. This sequence starts with short couplings (1:1) goes through longer coupled rhythm to finish again with a short coupling (2:2) and with irregularity windows in between. In our analysis, we showed that, for $h$ values higher than 26.95 ms, short stimulation periods produce a period-doubling bifurcation cascade that ends in chaotic behavior. Furthermore, subsequent stimulation period reduction leads to an inverse bifurcation cascade that ends in a 1-period rhythm, again with irregular behavior in between.

As we mentioned before, alternans are considered a cardiac risk predictor. In clinical examinations, alternant T-waves are generally not present without chronotropic challenge. Here we have shown, in a model for cardiac patient ventricle cells, that CRC with a local maximum advances the response to accelerated activation, as well as increasing the complexity of the system. However, it is not clear how this complex behavior propagates or influences the neighboring cells which may or may not have a monotonic CRC. A simulation considering an expanded range of CRC would be important for a better understanding of the evolution and dynamics of the CRC-LM and, hopefully, contribute in the development of a new type of indexes or cardiac risk metrics.

# References

1. J.M. Pastore, S.D. Girouard, K.R. Laurita, F.G. Akar, D.S. Rosenbaum, Mechanism linking T-wave alternans to the genesis of cardiac fibrillation. Circulation **99**, 1385–1394 (1999)
2. M.R. Guevara, G. Ward, A. Shrier, L. Glass, Electrical alternans and period doubling bifurcation. IEEE Comput. Cardiol. **167**, 18–24 (1984)
3. J.B. Nolasco, R.W. Dahlen, A graphic method for the study of alternation in cardiac action potentials. J. Appl. Physiol. **25**, 191–196 (1968)
4. M.R. Franz, The electrical restitution curve revisited: steep or flat slope—which is better? J. Cardiovasc. Electrophysiol. **14**, S140–S147 (2003)

5. J.N. Weiss, A. Garfinkel, H.S. Karagueuzian, T.P. Nguyen, R. Olcese, P.S. Chen, Z. Qu, Perspective: a dynamics-based classification of ventricular arrhythmias. J. Mol. Cell. Cardiol. **82**, 136–154 (2015)

6. P.N. Jordan, D.J. Christini, Determining the effects of memory and action potential duration alternans on cardiac restitution using a constant-memory restitution protocol. Physiol. Meas. **25**(4), 1013 (2004)

7. S.D. McIntyre, V. Kakade, Y. Mori, E.G. Tolkacheva, Heart rate variability and alternans formation in the heart: The role of feedback in cardiac dynamics. J. Theor. Biol. **350**, 90–97 (2014)

8. F. Fenton, E.M. Cherry, Cardiac Dynamics: Restitution (2012) http://www.scholarpedia.org/article/User:Flavio_H_Fenton/Proposed/Restitution

9. A. Garfinkel, Y.H. Kim, O. Voroshilovsky, Z. Qu, J.R. Kil, M.H. Lee, H.S. Karagueuzian, J.N. Weiss, P.S. Chen, Preventing ventricular fibrillation by flattening cardiac restitution. Proc. Natl. Acad. Sci. USA **97**, 6061–6066 (2000)

10. A. Karma, New paradigm for drug therapies of cardiac fibrillation. PNAS **97**(11) (2000)

11. M. Watanabe, N.F. Otani, R.F. Gilmour Jr, Biphasic restitution of action potential duration and complex dynamics in ventricular myocardium. Circ. Res. **76**, 915–921 (1995)

12. H. Dvir, S. Zlochiver, The Interrelations among stochastic pacing, stability, and memory in the Heart. Biophys. J. **107**, 1023–1034 (2014)

13. H. Jiang, D. Zhao, B. Cui, Z. Lu, J. Lü, F. Chen, M. Bao, Electrical restitution determined by epicardial contact mapping and surface electrocardiogram: its role in ventricular fibrillation inducibility in swine. J. Electrocardiol. **41**, 152–159 (2008)

14. B.C. Knollmann, T. Schober, A.O. Petersen, S.G. Sirenko, M.R. Franz, Action potential characterization in intact mouse heart: steady-state cycle length dependence and electrical restitution. Am. J. Physiol.- Heart Circul. Physiol. **292**(1), H614–H621 (2006). doi:10.1152/ajpheart.01085.2005

15. M. Watanabe, D.P. Zipes, R.F. Gilmour Jr, Oscillations of diastolic interval and refractory period following premature and postmature stimuli in canine cardiac Purkinje fibers. Pacing Clin. Electrophysiol. **12**, 1089–1103 (1989)

16. R. Wu, A. Patwardhan, Restitution of action potential duration during sequential changes in diastolic intervals shows multimodal behavior. Circ. Res. **96**, 634–641 (2012)

17. M.R. Guevara, L. Glass, A. Shrier, Phase locking, period-doubling bifurcations, and irregular dynamics in periodically stimulated cardiac cells. Science **214**, 1350–1353 (1981)

18. G.M. Hall, S. Bahar, D.J. Gauthier, Prevalence of rate-dependent behaviors in cardiac muscle. Phys. Rev. Lett. **82**, 2995 (1999)

19. A. Karma, Electrical alternans and spiral wave breakup in cardiac tissue. Chaos **4**, 461–72 (1994)

20. O.E. Osadchii, Effects of ventricular pacing protocol on electrical restitution assessments in guinea-pig heart. Exp. Physiol. **97**(7), 807–821 (2012)

21. H. Arce, A. Xu, H. González, M.R. Guevara, Alternans and higher-order rhythms in an ionic model of a sheet of ischemic ventricular muscle. Chaos **10**(2), 411 (2000)

22. B.J. Bas, Restitution of the action potential in cat papillary muscle. J. Physiol. **228**, 1717–1724 (1975)

23. M.R. Franz, C.D. Swerdlow, L.B. Liem, J. Schaefer, Cycle length dependence of human action potential duration in vivo. J. Clin. Investig. **82**(3), 972–979 (1988)

24. A.M. Yue, M.R. Franz, P.R. Roberts, J.M. Morgan, Global endocardial electrical restitution in human right and left ventricles determined by noncontact mapping. J. Am. Coll. Cardiol. **46**(6), 1067 (2005)

25. L.L. Trulla, A. Giuliani, J.P. Zbilut, C.L. Webber Jr, Recurrence quantification analysis of the logistic equation with transients. Phys. Lett. A **223**(4), 255–260 (1996)

26. J. Gao, Recurrence time statistics for chaotic systems and their applications. Phys. Rev. Lett. **83**(16), 3178–3181 (1999)

27. J.P. Eckmann, S.O. Kamphorst, D. Ruelle, S. Ciliberto, Liapunov exponents from time series. Phys. Rev. A **34**(6), 4971–4979 (1986)

28. C.L. Webber Jr, J.P. Zbilut, Dynamical assessment of physiological systems and states using recurrence plot strategies. J. Appl. Physiol. **76**, 965–973 (1994)
29. J.P. Zbilut, C.L. Webber Jr, Embeddings and delays as derived from quantification of recurrence plots. Phys. Lett. A **171**, 199–203 (1992). doi:10.1161/01.CIR.99.10.1385
30. N. Marwan, N. Wessel, U. Meyerfeldt, A. Schirdewan, J. Kurths, Recurrence plot based measures of complexity and its application to heart rate variability data. Phys. Rev. E **66**(2), 026702 (2002)
31. N. Marwan, C.M. Romano, M. Thiel, J. Kurths, Recurrence plots for the analysis of complex systems. Phys. Rep. **438**(5–6), 237–329 (2007)
32. E.M. Oblow, Supertracks, supertrack functions and chaos in the quadratic map. Phys. Lett. A **128**(8), 406–412 (1988). doi:10.1016/0375-9601(88)90119-3